Innervation density governs crosstalk of GPCR-based norepinephrine and dopamine sensors

Ricardo C. López[1], Natalie Noble[1]*, Özge D. Özçete[1]*, Xintong Cai[1], Gillian E. Handy[1], Jonathan W. Andersen[1], Tommaso Patriarchi[2,3], Yulong Li[4], and Pascal S. Kaeser[1,#]

[1]Department of Neurobiology, Harvard Medical School, Boston, United States

[2]Institute of Pharmacology and Toxicology, University of Zürich, Zürich, Switzerland

[3]Neuroscience Center Zürich, ETH and University of Zürich, Zürich, Switzerland

[4]State Key Laboratory of Membrane Biology, Peking University School of Life Sciences, Beijing, China

* equal contribution

[#] correspondence: kaeser@hms.harvard.edu

Summary

GPCR-based fluorescent sensors are widely used to correlate neuromodulatory signaling with brain function. While experiments in transfected cells often reveal selectivity for individual neurotransmitters, sensor specificity in the brain frequently remains uncertain. Pursuing experiments in brain slices and in vivo, we find that norepinephrine and dopamine cross-activate the respective sensors. Non-specific activation occurred when innervation of the cross-reacting transmitter was high, and silencing of specific innervation was indispensable for interpreting sensor fluorescence.

Main

G protein-coupled receptor (GPCR)-based fluorescent sensors have revolutionized our means of studying neuromodulatory signaling in the brain. Their ability to discriminate neurotransmitters relies on the properties of the respective endogenous GPCRs that are used for sensor engineering. Studies describing new sensors typically measure EC_{50} values in transfected cells by comparing responses to locally puffed neurotransmitters at increasing concentrations[1–6]. While this approach generally finds high specificity, it is often unclear how this in vitro selectivity translates to the brain. In addition to sensor affinities, local innervation densities of neuromodulatory axons and the organization of release and reuptake machinery may strongly influence which transmitters are reported by a given indicator. This is particularly relevant for transmitters with similar chemical structures.

We examined the selectivity of GPCR-based norepinephrine and dopamine sensors[2,4,5] that are widely used, often in brain areas innervated by both transmitter systems (Supplemental text). We first quantified the innervation densities of these transmitters in primary motor cortex (M1) and dorsal striatum. Prior work has found dense dopamine innervation in dorsal striatum and prominent presence of norepinephrine axons in M1 cortex[7–11]. To measure axonal densities, we genetically labeled dopamine axons by Cre-dependent expression of synaptophysin-tdTomato in DAT[IRES-Cre] mice (Fig. 1a-c, Supplemental fig. 1). We prepared brain slices containing dorsal striatum and M1 cortex and performed antibody staining against RFP and the norepinephrine transporter (NET) to visualize dopamine and norepinephrine axons, respectively (Fig. 1b+c). Confocal images revealed segregation of the two fluorescence signals within each area. In M1 cortex, norepinephrine fibers predominated, and dopamine fibers were sparse. Conversely, dopamine axons were dense in dorsal striatum while norepinephrine axons were infrequent. Quantification of each signal suggested that M1 cortex contains ~15 times more norepinephrine

3

than dopamine innervation, and dorsal striatum as much as ~350 times more dopamine than NET-stained innervation (Fig. 1c). Assessment of staining in the locus coeruleus (LC) and substantia nigra pars compacta, the corresponding sites of norepinephrine and dopamine neuron somata, confirmed the specificity of the genetic strategy (Supplemental fig. 1).

To examine the transmitter dynamics resulting from these innervation patterns, we first expressed the norepinephrine sensor $GRAB_{NE2h}$ (α2 adrenergic receptor-based, abbreviated as $GRAB_{NE}$)[4] in M1 cortex or dorsal striatum and analyzed evoked fluorescence transients in acute brain slices with widefield microscopy (Fig. 1d-j). Single electrical stimuli and stimulus trains (20 stimuli at 20 Hz) yielded fluorescence increases in M1 cortex consistent with norepinephrine innervation (Fig. 1e-g). These transients were fully blocked by inhibition of action potential firing but persisted in a cocktail of blockers of synaptic transmission (Supplemental fig. 2). Single stimuli induced small $GRAB_{NE}$ transients, and 20-stimulus trains produced a buildup with a peak amplitude ~5 times greater than that of a single stimulus (Fig. 1f+g), similar to prior electrochemical studies[9,12,13]. Robust $GRAB_{NE}$ transients were also detected in the dorsal striatum despite the near absent norepinephrine innervation, though with different properties (Fig. 1h-j). Peak striatal $GRAB_{NE}$ transients were similar between single and train stimuli, and they decayed more rapidly than the transients in M1 cortex.

The distinct innervation patterns and $GRAB_{NE}$ signals in M1 cortex and dorsal striatum (Fig. 1) suggest that $GRAB_{NE}$ might report dopamine in the striatum. This is further supported by the similarity of striatal $GRAB_{NE}$ transients (Fig. 1h-j) to the properties of dopamine release[14–16]. The initial characterization of $GRAB_{NE}$ found an EC_{50} of ~190 nM for norepinephrine and ~9 μM for dopamine[4]. Correspondingly, the $GRAB_{NE}$ response in transfected cells was ~10-fold greater for 10 μM norepinephrine puffs compared to 10 μM dopamine puffs (Supplemental fig. 3). Dopamine-laden vesicles, though, have an intravesicular dopamine concentration of up to ~1 M,

and the dopamine concentration at the pore of a fusing vesicle[9,17,18] far exceeds commonly used concentrations for probing selectivity[1–6].

To directly test whether dopamine induces $GRAB_{NE}$ transients in dorsal striatum, we used mice with conditional deletion of the release site-organizer protein RIM in dopamine neurons (RIM cKO^{DA}, Fig. 2a+b). In these mutants, evoked dopamine release is disrupted when assessed with amperometry, whole-cell electrophysiology, or $GRAB_{DA}$[14,16,19,20]. Striatal slices from RIM cKO^{DA} mice displayed strong reductions in evoked $GRAB_{NE}$ transients compared to RIM control slices in response to both single and train stimuli (Fig. 2c-e). The same was true when nicotinic acetylcholine receptors, which trigger dopamine release via induction of dopamine axonal action potentials[21–23], were blocked (Supplemental fig. 4). We next used nLightG, an alternate GPCR-based norepinephrine sensor engineered from the α1 adrenergic receptor[5]. Like $GRAB_{NE}$, nLightG also reported striatal dopamine release (Fig. 2f-h), though with several fold lower overall amplitudes. RIM cKO^{DA} slices had ~90% reduced nLightG responses, a reduction similar to that observed with $GRAB_{NE}$.

To test whether the cross-reactivity is also present in vivo and detected in response to endogenous neural activity, we performed fiber photometric $GRAB_{NE}$ recordings in freely moving RIM control and RIM cKO^{DA} mice (Fig. 2i-k, Supplemental fig. 5). Fluorescence transients were measured as mice explored an open field arena, and we quantified $GRAB_{NE}$ fluctuations as variation of $\Delta F/F_0$. $GRAB_{NE}$ fluctuations were readily detected in RIM control mice, but nearly absent in RIM cKO^{DA} mice (Fig. 2j+k). This is similar to striatal transients measured with dopamine sensors[16]. In summary, these data establish that two commonly used norepinephrine sensors are almost exclusively activated by dopamine in the dorsal striatum.

Given the robust cortical norepinephrine innervation, we next examined the ability of $GRAB_{NE}$

5

and nLightG to detect norepinephrine in M1 cortex. We first established that chemical lesion of norepinephrine neurons in the right LC with 6-hydroxydopamine (6-OHDA)[24] abolished cortical NET staining in the same hemisphere (Fig. 3a-c, Supplemental Fig. 6). We then bilaterally expressed GRAB$_{NE}$ or nLightG in M1 cortex in mice with unilateral LC lesions (Fig. 3d+h). Both sensors showed increased fluorescence in response to single and train stimuli and in each case, the transients were strongly decreased when the LC was lesioned (Fig. 3d-k). Importantly, striatal GRAB$_{NE}$ responses were not impaired after LC lesion (Supplemental fig. 6c-f), indicating that they did not arise from LC neurons and that dopamine neurons were not lesioned by 6-OHDA injection into the LC.

Given the structural similarities of dopamine and norepinephrine, do dopamine sensors detect norepinephrine? We tested GRAB$_{DA2m}$, a commonly used D2 receptor-based sensor (abbreviated as GRAB$_{DA}$) with an EC$_{50}$ of ~80 nM and ~1.2 µM for dopamine and norepinephrine, respectively[2]. In transfected HEK293T cells, puffing 10 µM dopamine or norepinephrine produced similar GRAB$_{DA}$ fluorescence changes (Supplemental fig. 7). We have previously shown that striatal GRAB$_{DA}$ transients are strongly impaired in RIM cKO^{DA} mice[16], establishing that GRAB$_{DA}$ reports dopamine in the striatum. When we monitored GRAB$_{DA}$ signals in M1 cortex (Fig. 3l-o), transients induced by single and train stimuli were impaired by ~50% following 6-OHDA lesion of LC. Hence, GRAB$_{DA}$ responds at least partially to norepinephrine in M1 cortex. The remaining transients may be due to cortical dopamine innervation, which may be enhanced upon LC ablation[24], or to other transmitters.

The LC receives hardly any dopamine innervation (Supplemental fig. 1)[10]. To evaluate transmitter dynamics in the LC, we expressed either GRAB$_{NE}$ or GRAB$_{DA}$ bilaterally in the LC and monitored fluorescence transients. Evoked LC GRAB$_{NE}$ transients had similar characteristics (Supplemental fig. 8a-d) to those measured in cortex (Fig. 1d-g), and so did LC

6

GRAB$_{DA}$ transients (Supplemental fig. 8e-g). With both sensors, single pulse transients were small compared to those produced by 20 stimuli at 20 Hz, and the transients had prolonged decays. These findings suggest that GRAB$_{DA}$ and GRAB$_{NE}$ report norepinephrine in LC.

The presented results establish that GPCR-based norepinephrine and dopamine sensors have prominent crosstalk in the brain. Although in vitro affinity measurements reflect sensor properties, a key determinant of sensor activation in the brain is the ratio of axonal innervation densities of specific modulators, which can vary by 100-fold or more between different brain areas (Fig. 1). Our findings are important for many past and ongoing studies (Supplemental text). Typically, sensor transients are interpreted as reporting the transmitter they were named after, and appropriate loss-of-function experiments are often not performed. A commonly used control to verify sensor activation is pharmacological sensor inhibition, though this approach does not validate transmitter specificity. We propose that crosstalk should always be experimentally addressed in studies using GPCR-based sensors for neuromodulatory transmitters. To this end, genetic or chemical silencing are essential to interpret sensor signals in brain slices and in vivo. These manipulations should be done under the specific conditions used in a study and are a necessary standard in the future.

The cross-reactivity we observe for dopamine and norepinephrine sensors is unlikely limited to these two transmitters. Many modulators, including serotonin, other monoamines, and more than a hundred neuropeptides operate in the brain[9], and these systems might cross-activate a variety of sensors. Achieving full signal selectivity is particularly challenging based on the structural similarities of some of these transmitters.

Synthesis pathways might further complicate the interpretation of catecholamine sensor data. For example, neurons synthesize norepinephrine through enzymatic conversion of dopamine,

7

and LC neurons might co-release dopamine and norepinephrine[25,26]. Thus, the sensors might report mixed signals in response to activities of norepinephrine neurons when enzymatic conversion is incomplete.

Finally, we note that cross-talk is not a "flaw" of the sensors but instead reflects the properties of GPCRs. Dopamine and adrenergic receptors, for example, can bind both dopamine and norepinephrine[27–29]. Receptors for other neuromodulators also interact with several ligands[30–32]. While this non-selectivity complicates interpretations of sensor imaging and fiber photometry, it underscores that receptor crosstalk likely represents a biologically meaningful mechanism to convey information and to regulate cells, circuits, and behavior.

Acknowledgements

Author contributions

Conceptualization: R.C.L. and P.S.K.; Methodology: R.C.L., N. N., O.D.O., X.C., J.W.A.; Resources: X.C., G.E.H., T.P., Y.L.; Investigation: R.C.L., N.N.; Formal Analysis: R.C.L., N.N.; Writing-Original Draft: R.C.L. and P.S.K.; Writing - Review and Editing: R.C.L., N.N., O.D.O., X.C., J.W.A., G.E.H., T.P., Y.L., P.S.K.; Supervision: P.S.K.; Funding Acquisition: P.S.K.

Declaration of interests

YL is listed as an inventor on a patent application (PCT/CN2018/107533) describing GPCR-based probes. TP is listed as an inventor on a patent application (PCT/US17/62993) describing GPCR-based probes. The other authors declare no competing interests.
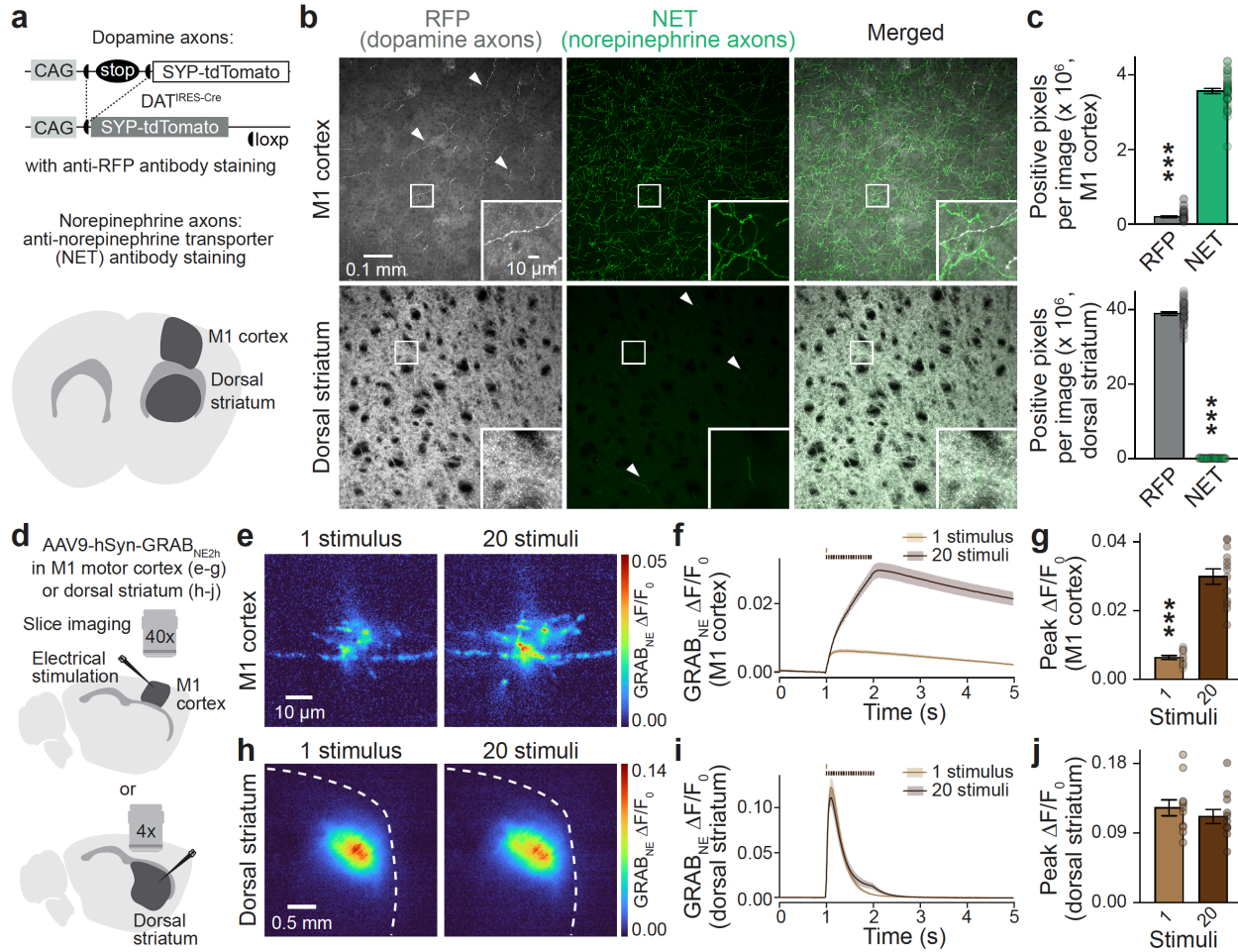
Figure 1. Cortex and striatum have distinct dopamine and norepinephrine innervation and GRAB$_{NE}$ dynamics

a. Strategy for quantification of dopamine and norepinephrine innervation with confocal microscopy. Dopamine axons were labeled by anti-red fluorescent protein (RFP) antibody staining in coronal brain slices of DAT$^{IRES-Cre}$ mice with Cre-dependent synaptophysin-tdTomato (SYP-tdTomato) expression. Norepinephrine axons were labeled with anti-norepinephrine transporter (NET) antibodies.

b, c. Representative images of M1 cortex and dorsal striatum (b) and quantification of RFP and NET staining (c) as the total number of positive pixels in image stacks after binarization. In b, brightness and contrast in the gray (RFP) channel were differentially adjusted to render cortical dopamine axons visible and to prevent saturation of dorsal striatum; M1 cortex 40 slices from 8

10

mice, dorsal striatum 40/8.

d. Schematic of imaging in acute sagittal slices containing M1 cortex and dorsal striatum. Wide-field fluorescence imaging was performed 3 weeks after stereotaxic AAV injections of the corresponding brain areas to express GRAB$_{NE}$. Electrical stimulation was used to elicit fluorescence transients.

e-j. Representative images of peak GRAB$_{NE}$ fluorescence in response to 1 stimulus or 20 stimuli at 20 Hz in M1 cortex (e) or dorsal striatum (h) and quantification of GRAB$_{NE}$ $\Delta F/F_0$ time series (f, i) and peak $\Delta F/F_0$ (g, j); M1 cortex 13 slices from 3 mice, dorsal striatum 11/3.

Data are mean ± SEM; *** $p < 0.001$, as assessed by: two-tailed Mann-Whitney rank-sum test in c, two-tailed Wilcoxon signed-rank test in g. For assessment of somatic stainings in LC and SNc, see Supplemental fig. 1. For pharmacological blockade of GRAB$_{NE}$ transients in brain slices, see Supplemental fig. 2. For assessment of GRAB$_{NE}$ in HEK293T cells, see Supplemental fig. 3.
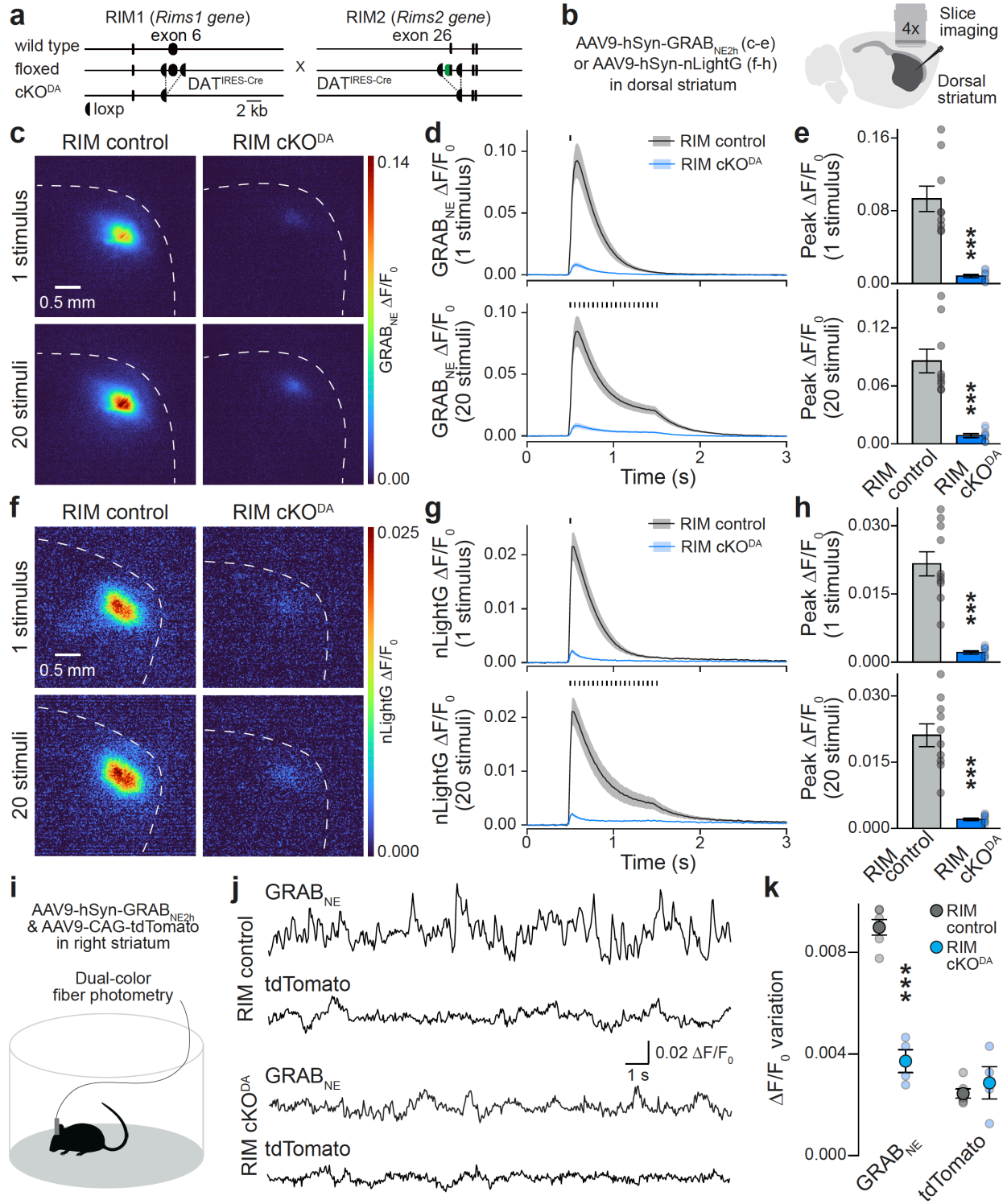
Figure 2. Norepinephrine sensors detect dopamine in dorsal striatum

a. Strategy for conditional deletion of RIM1 and RIM2 in dopamine neurons as established before[14,16,19,20].

b. Schematic of slice imaging in dorsal striatum after expressing $GRAB_{NE}$ or nLightG.

c-e. Representative images of peak $GRAB_{NE}$ fluorescence in response to 1 stimulus or 20 stimuli at 20 Hz (c) and quantification of $GRAB_{NE}$ $\Delta F/F_0$ time series (d) and peak $\Delta F/F_0$ (e); RIM control 9 slices from 3 mice, RIM cKO^{DA} 9/3.

f-h. As in c-e, but with nLightG instead of $GRAB_{NE}$; RIM control 10/3, RIM cKO^{DA} 10/3.

i. Schematic of fiber photometry in freely moving mice co-expressing $GRAB_{NE}$ and tdTomato in the right dorsal striatum.

j, k. Representative examples of $GRAB_{NE}$ and tdTomato $\Delta F/F_0$ (j) and fluorescence variation quantified as standard deviation (SD) of $GRAB_{NE}$ and tdTomato $\Delta F/F_0$ (k); RIM control 6 mice, RIM cKO^{DA} 4.

Data are mean ± SEM; *** $p < 0.001$, as assessed by: two-tailed Mann-Whitney rank-sum tests in e and h, two-tailed unpaired t-test in k. For assessment of striatal $GRAB_{NE}$ transients while blocking nicotinic acetylcholine receptors, see Supplemental fig. 4. For post-hoc assessment of fiberoptic cannula positions, see Supplemental fig. 5.

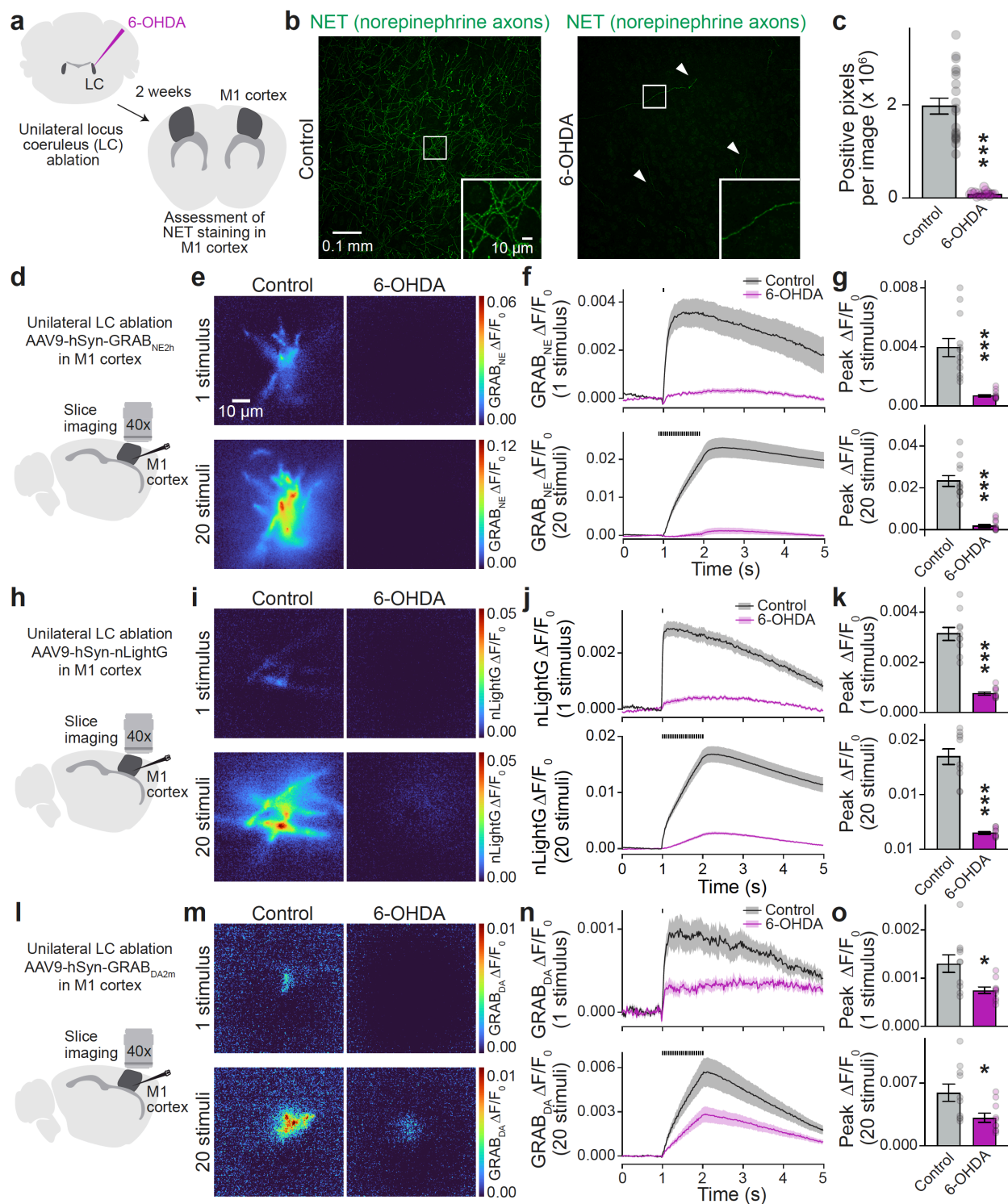**Figure 3. Norepinephrine and dopamine sensors in M1 cortex**

a. Schematic of unilateral LC ablation with 6-OHDA. Two weeks after injection, norepinephrine axons were labeled with anti-NET antibodies. Analyses were performed on confocal images of

coronal sections in contralateral (control) and ipsilateral (6-OHDA) hemispheres.

b, c. Representative images of M1 cortex (b) and quantification of NET signals (c); 20 slices from 4 mice.

d. Schematic of bilateral slice imaging in M1 cortex expressing GRAB$_{NE}$ following unilateral ablation of the right LC.

e-g. Representative images of peak GRAB$_{NE}$ fluorescence in response to 1 stimulus or 20 stimuli at 20 Hz in ipsilateral (6-OHDA) and contralateral (control) hemispheres (e) and quantification of GRAB$_{NE}$ $\Delta F/F_0$ time series (f) and peak $\Delta F/F_0$ (g); control 12 slices from 3 mice, 6-OHDA 12/3.

h-k. As in d-g, but with nLightG instead of GRAB$_{NE}$; control 10/3, 6-OHDA 10/3.

l-o. As in d-g, but with GRAB$_{DA}$ instead of GRAB$_{NE}$; control 10/3, 6-OHDA 10/3.

Data are mean ± SEM; *** $p < 0.001$, * < 0.05 as assessed by: two-tailed Mann-Whitney rank-sum tests in c, g, k, and o (1 stimulus); two-tailed unpaired t-test in o (20 stimuli). For assessment of histology and GRAB$_{NE}$ responses in striatum following 6-OHDA injection in LC, see Supplemental fig. 6. For assessment of GRAB$_{DA}$ in HEK293T cells, see Supplemental fig. 7. For assessment of GRAB$_{NE}$ and GRAB$_{DA}$ transients in LC, see Supplemental fig. 8.

References

1. Sun, F. *et al.* A Genetically Encoded Fluorescent Sensor Enables Rapid and Specific Detection of Dopamine in Flies, Fish, and Mice. *Cell* **174**, 481-496.e19 (2018).

2. Sun, F. *et al.* Next-generation GRAB sensors for monitoring dopaminergic activity in vivo. *Nat Methods* **17**, 1156–1166 (2020).

3. Zhuo, Y. *et al.* Improved green and red GRAB sensors for monitoring dopaminergic activity in vivo. *Nat Methods* **21**, 680–691 (2024).

4. Feng, J. *et al.* Monitoring norepinephrine release in vivo using next-generation GRABNE sensors. *Neuron* 2023.06.22.546075 (2024) doi:10.1016/j.neuron.2024.03.001.

5. Kagiampaki, Z. *et al.* Sensitive multicolor indicators for monitoring norepinephrine in vivo. *Nat Methods* **20**, 1426–1436 (2023).

6. Wu, Z., Lin, D. & Li, Y. Pushing the frontiers: tools for monitoring neurotransmitters and neuromodulators. *Nat Rev Neurosci* **23**, 257–274 (2022).

7. Plummer, N. W. *et al.* An Intersectional Viral-Genetic Method for Fluorescent Tracing of Axon Collaterals Reveals Details of Noradrenergic Locus Coeruleus Structure. *eNeuro* **7**, (2020).

8. Matsuda, W. *et al.* Single nigrostriatal dopaminergic neurons form widely spread and highly dense axonal arborizations in the neostriatum. *J Neurosci* **29**, 444–53 (2009).

9. Özçete, Ö. D., Banerjee, A. & Kaeser, P. S. Mechanisms of neuromodulatory volume transmission. *Mol Psychiatry* **193**, 73–88 (2024).

10. Schwarz, L. A. *et al.* Viral-genetic tracing of the input-output organization of a central noradrenaline circuit. *Nature* **524**, 88–92 (2015).

11. Chandler, D. J., Gao, W. J. & Waterhouse, B. D. Heterogeneous organization of the locus coeruleus projections to prefrontal and motor cortices. *Proc Natl Acad Sci U S A* **111**, 6816–6821 (2014).

12. Park, J., Takmakov, P. & Wightman, R. M. In vivo comparison of norepinephrine and dopamine release in rat brain by simultaneous measurements with fast-scan cyclic voltammetry. *J Neurochem* **119**, 932–944 (2011).

13. Park, J., Kile, B. M. & Wightman, M. R. In vivo voltammetric monitoring of norepinephrine release in the rat ventral bed nucleus of the stria terminalis and anteroventral thalamic nucleus. *Eur J Neurosci* **30**, 2121–2133 (2009).

14. Liu, C., Kershberg, L., Wang, J., Schneeberger, S. & Kaeser, P. S. Dopamine Secretion Is Mediated by Sparse Active Zone-like Release Sites. *Cell* **172**, 706-718.e15 (2018).

15. Marcott, P. F., Mamaligas, A. A. & Ford, C. P. Phasic Dopamine Release Drives Rapid Activation of Striatal D2-Receptors. *Neuron* **84**, 164–176 (2014).

16. Cai, X. *et al.* Dopamine dynamics are dispensable for movement but promote reward responses. *Nature* (2024) doi:10.1038/s41586-024-08038-z.

17. Omiatek, D. M. *et al.* The real catecholamine content of secretory vesicles in the CNS revealed by electrochemical cytometry. *Sci Rep* **3**, 1447 (2013).

18. Garris, P., Ciolkowski, E., Pastore, P. & Wightman, R. Efflux of dopamine from the synaptic cleft in the nucleus accumbens of the rat brain. *The Journal of Neuroscience* **14**, 6084–6093 (1994).

19. Robinson, B. G. *et al.* RIM is essential for stimulated but not spontaneous somatodendritic dopamine release in the midbrain. *Elife* **8**, (2019).

20. Banerjee, A. *et al.* Molecular and functional architecture of striatal dopamine release sites. *Neuron* **110**, 248-265.e9 (2022).

21. Soliakov, L. & Wonnacott, S. Voltage-sensitive Ca2+ channels involved in nicotinic receptor-mediated [3H]dopamine release from rat striatal synaptosomes. *J Neurochem* **67**, 163–70 (1996).

22.   Threlfell, S. *et al.* Striatal dopamine release is triggered by synchronized activity in cholinergic interneurons. *Neuron* **75**, 58–64 (2012).

23.   Liu, C. *et al.* An action potential initiation mechanism in distal axons for the control of dopamine release. *Science* **375**, 1378–1385 (2022).

24.   Harik, S. I. Locus ceruleus lesion by local 6-hydroxydopamine infusion causes marked and specific destruction of noradrenergic neurons, long-term depletion of norepinephrine and the enzymes that synthesize it, and enhanced dopaminergic mechanisms in the ipsilateral cerebral cortex. *J Neurosci* **4**, 699–707 (1984).

25.   Devoto, P., Flore, G., Saba, P., Fà, M. & Gessa, G. L. Co-release of noradrenaline and dopamine in the cerebral cortex elicited by single train and repeated train stimulation of the locus coeruleus. *BMC Neurosci* **6**, (2005).

26.   Smith, C. C. & Greene, R. W. CNS dopamine transmission mediated by noradrenergic innervation. *J Neurosci* **32**, 6072–6080 (2012).

27.   Aguayo, L. G. & Grossie, J. Dopamine inhibits a sustained calcium current through activation of alpha adrenergic receptors and a GTP-binding protein in adult rat sympathetic neurons. *J Pharmacol Exp Ther* **269**, 503–8 (1994).

28.   Root, D. H. *et al.* Norepinephrine activates dopamine D4 receptors in the rat lateral habenula. *J Neurosci* **35**, 3460–3469 (2015).

29.   Sánchez-Soto, M. *et al.* Evidence for Noncanonical Neurotransmitter Activation: Norepinephrine as a Dopamine D2-Like Receptor Agonist. *Mol Pharmacol* **89**, 457–466 (2016).

30.   Oz, M., Zhang, L., Rotondo, A., Sun, H. & Morales, M. Direct activation by dopamine of recombinant human 5-HT1A receptors: comparison with human 5-HT2C and 5-HT3 receptors. *Synapse* **50**, 303–313 (2003).

31.   Piper, S. J. *et al.* Understanding VPAC receptor family peptide binding and selectivity. *Nat Commun* **13**, (2022).

32.   Song, Z. & Albers, H. E. Cross-talk among oxytocin and arginine-vasopressin receptors: Relevance for basic and clinical studies of the brain and periphery. *Front Neuroendocrinol* **51**, 14–24 (2018).

33.   Backman, C. M. *et al.* Characterization of a mouse strain expressing Cre recombinase from the 3' untranslated region of the dopamine transporter locus. *Genesis* **44**, 383–390 (2006).

34.   Kaeser, P. S. *et al.* RIM1alpha and RIM1beta are synthesized from distinct promoters of the RIM1 gene to mediate differential but overlapping synaptic functions. *J Neurosci* **28**, 13435–13447 (2008).

35.   Kaeser, P. S. *et al.* RIM proteins tether Ca2+ channels to presynaptic active zones via a direct PDZ-domain interaction. *Cell* **144**, 282–95 (2011).

36.   Tan, C., Wang, S. S. H., de Nola, G. & Kaeser, P. S. Rebuilding essential active zone functions within a synapse. *Neuron* **110**, 1498-1515.e8 (2022).

37.   Chin, M. & Kaeser, P. S. The intracellular C-terminus confers compartment-specific targeting of voltage-gated calcium channels. *Cell Rep* **43**, 114428 (2024).

38.   Franklin, K. P. J. & Paxinos, G. *The Mouse Brain in Stereotaxic Coordinates.* (Elsevier, 2007).

39.   Chantranupong, L. *et al.* Dopamine and glutamate regulate striatal acetylcholine in decision-making. *Nature* **621**, 577–585 (2023).

40.   Basu, A. *et al.* Frontal Norepinephrine Represents a Threat Prediction Error Under Uncertainty. *Biol Psychiatry* **96**, 256–267 (2024).

41.   Glaeser-Khan, S. *et al.* Spatiotemporal Organization of Prefrontal Norepinephrine Influences Neuronal Activity. *eNeuro* **11**, (2024).

42.   Kjaerby, C. *et al.* Memory-enhancing properties of sleep depend on the oscillatory amplitude of norepinephrine. *Nat Neurosci* **25**, 1059–1070 (2022).

17

43. Ma, C. *et al.* Microglia regulate sleep through calcium-dependent modulation of norepinephrine transmission. *Nat Neurosci* **27**, 249–258 (2024).

44. Pittolo, S. *et al.* Dopamine activates astrocytes in prefrontal cortex via α1-adrenergic receptors. *Cell Rep* **40**, (2022).

45. Saito, A. *et al.* Social defeat stress enhances the rewarding effects of cocaine through α1A adrenoceptors in the medial prefrontal cortex of mice. *Neuropharmacology* **242**, (2024).

46. Yang, J.-H. *et al.* Frontal cortex norepinephrine, serotonin, and dopamine dynamics in an innate fear-reward behavioral model. *bioRxiv* 2023.11.27.568929 (2023) doi:10.1101/2023.11.27.568929.

47. Breton-Provencher, V., Drummond, G. T., Feng, J., Li, Y. & Sur, M. Spatiotemporal dynamics of noradrenaline during learned behaviour. *Nature* **606**, 732–738 (2022).

48. Patriarchi, T. *et al.* Ultrafast neuronal imaging of dopamine dynamics with designed genetically encoded sensors. *Science (1979)* **360**, eaat4422 (2018).

49. Grove, J. C. R. *et al.* Dopamine subsystems that track internal states. *Nature* **608**, 374–380 (2022).

50. Labouesse, M. A. *et al.* A chemogenetic approach for dopamine imaging with tunable sensitivity. *Nat Commun* **15**, (2024).

51. Canton-Josh, J. E., Qin, J., Salvo, J. & Kozorovitskiy, Y. Dopaminergic regulation of vestibulo-cerebellar circuits through unipolar brush cells. *Elife* **11**, (2022).

52. Tsetsenis, T. *et al.* Midbrain dopaminergic innervation of the hippocampus is sufficient to modulate formation of aversive memories. *Proc Natl Acad Sci U S A* **118**, (2021).

53. Sayegh, F. J. P. *et al.* Ventral tegmental area dopamine projections to the hippocampus trigger long-term potentiation and contextual learning. *Nat Commun* **15**, (2024).

54. Korchynska, S. *et al.* A hypothalamic dopamine locus for psychostimulant-induced hyperlocomotion in mice. *Nat Commun* **13**, (2022).

55. Lerner, T. N. *et al.* Intact-Brain Analyses Reveal Distinct Information Carried by SNc Dopamine Subcircuits. *Cell* **162**, 635–647 (2015).

56. Lutas, A., Fernando, K., Zhang, S. X., Sambangi, A. & Andermann, M. L. History-dependent dopamine release increases cAMP levels in most basal amygdala glutamatergic neurons to control learning. *Cell Rep* **38**, (2022).

57. Privitera, M. *et al.* Noradrenaline release from the locus coeruleus shapes stress-induced hippocampal gene expression. *Elife* **12**, (2024).

58. Wilmot, J. H. *et al.* Phasic locus coeruleus activity enhances trace fear conditioning by increasing dopamine release in the hippocampus. *Elife* **12**, (2024).

59. Wilson, L. R. *et al.* Partial or Complete Loss of Norepinephrine Differentially Alters Contextual Fear and Catecholamine Release Dynamics in Hippocampal CA1. *Biological psychiatry global open science* **4**, 51–60 (2023).

60. Feng, J. *et al.* A Genetically Encoded Fluorescent Sensor for Rapid and Specific In Vivo Detection of Norepinephrine. *Neuron* **102**, 745-761.e8 (2019).

61. Zhang, S. X. *et al.* Hypothalamic dopamine neurons motivate mating through persistent cAMP signalling. *Nature* **597**, 245–249 (2021).

62. Harada, M., Capdevila, L. S., Wilhelm, M., Burdakov, D. & Patriarchi, T. Stimulation of VTA dopamine inputs to LH upregulates orexin neuronal activity in a DRD2-dependent manner. *Elife* **12**, (2024).

63. Li, L. *et al.* Activity-dependent constraints on catecholamine signaling. *Cell Rep* **42**, (2023).

64. Agster, K. L., Mejias-Aponte, C. A., Clark, B. D. & Waterhouse, B. D. Evidence for a regional specificity in the density and distribution of noradrenergic varicosities in rat cortex. *J Comp Neurol* **521**, 2195–2207 (2013).

65. Beier, K. T. *et al.* Circuit Architecture of VTA Dopamine Neurons Revealed by Systematic Input-Output Mapping. *Cell* **162**, 622–634 (2015).

66. Augustine, V. *et al.* Temporally and Spatially Distinct Thirst Satiation Signals. *Neuron* **103**, 242-249.e4 (2019).

67. Bayless, D. W. *et al.* A neural circuit for male sexual behavior and reward. *Cell* **186**, 3862-3881.e28 (2023).

68. de Jong, J. W. *et al.* A Neural Circuit Mechanism for Encoding Aversive Stimuli in the Mesolimbic Dopamine System. *Neuron* **101**, 133-151.e7 (2019).

69. Mohebi, A., Wei, W., Pelattini, L., Kim, K. & Berke, J. D. Dopamine transients follow a striatal gradient of reward time horizons. *Nat Neurosci* **27**, 737–746 (2024).

70. Patriarchi, T. *et al.* An expanded palette of dopamine sensors for multiplex imaging in vivo. *Nat Methods* **17**, 1147–1155 (2020).

71. Salinas-Hernández, X. I., Zafiri, D., Sigurdsson, T. & Duvarci, S. Functional architecture of dopamine neurons driving fear extinction learning. *Neuron* **111**, 3854-3870.e5 (2023).

72. Vu, M. A. T. *et al.* Targeted micro-fiber arrays for measuring and manipulating localized multi-scale neural dynamics over large, deep brain volumes during behavior. *Neuron* **112**, 909-923.e9 (2024).

Methods

Mice

For morphological experiments, DAT[IRES-Cre] mice (RRID:IMSR_JAX:006660, B6.SJL-Slc6a3[tm1.1(cre)Bkmn]/J)[33] were bred to mice containing a CAG promoter-driven loxP-STOP-loxP-synaptophysin-tdTomato cassette (SYP-tdTomato) in the *Rosa26* locus (RRID: IMSR_JAX:012570, B6;129S-Gt(ROSA)26Sor[tm34.1(CAG-Syp/tdTomato)Hze]/J) as established before[14]. For conditional gene knockout experiments, mice carrying floxed alleles for RIM1 (RRID:IMSR_JAX:015832, Rims1[tm3Sud]/J)[34] and RIM2 (RRID:IMSR_JAX:015833, Rims2[tm1.1Sud]/J)[35] were bred to DAT[IRES-Cre] mice[33] as previously established[14,16,19,20]. RIM cKO[DA] mice were homozygous for floxed RIM1 and RIM2 and heterozygous for DAT[IRES-Cre]. RIM control mice were heterozygous for both floxed RIM alleles and DAT[IRES-Cre] and were either paired littermates of the experimental mice or age-matched non-littermate mice from intercrosses of the same alleles. Mice used for non-mutant comparisons were either wild type mice or contained floxed RIM1 and RIM2 alleles but were negative for DAT[IRES-Cre]. Male and female mice were included in all experiments regardless of sex. Intracranial injections for viral expression were performed at 5 to 12 weeks of age while functional and morphological analyses were performed at 8 to 17 weeks of age. Mice were maintained on a mixed background (containing C57BL/6 and 129/Sv) and housed in a room set to 20 to 24 ºC and 50% humidity. Mice used for fiber photometry were housed in a reversed light-dark cycle, and experiments were performed during the dark phases. Genotype comparisons were performed by an experimenter blind to genotype during data acquisition and analyses. Experiments followed approved protocols of the Harvard University Institutional Animal Care and Use Committee.

Confocal image acquisition and processing

Morphological analyses were adapted from protocols used previously[14,16,19,20]. Mice were deeply

anesthetized with 5% isoflurane and transcardially perfused with 30 mL of phosphate-buffered saline (PBS) followed by 40 mL of 4% paraformaldehyde (PFA) in PBS. Brains were post-fixed in 4% PFA in PBS for 24 hours and stored in PBS until sectioning. Mice with stereotaxic 6-OHDA injections were perfused two weeks following the injection. 50 μm thick brain slices were prepared in ice-cold PBS using a vibratome. Antigen retrieval was performed for 30 minutes at 60 ºC in a solution containing (in mM) 150 NaCl, 10 Tris Base, 1 EDTA, and 0.05% Tween 20 (pH 9.0). Slices were then permeabilized in PBS containing 0.25% Triton X-100 (PBST) in three consecutive 10-minute incubations at room temperature and blocked in PBST containing 10% normal goat serum for 2 hours at room temperature. Staining with primary antibodies was performed for 24 hours at 4 ºC in PBST with 10% normal goat serum. Sections were then washed three times for 10 minutes in PBST, followed by secondary antibody staining for 2 hours at room temperature in PBST with 10% normal goat serum. After another three 10-minute washes, the slices were mounted on glass slides for imaging. The primary antibodies used were mouse IgG1 anti-NET (1:1000 Synaptic Systems #260 011, RRID:AB_2636907, lab antibody code A265), guinea pig anti-RFP (1:1000, Synaptic Systems #390 004, RRID:AB_2737052, A258), and rabbit anti-TH (1:2000, Millipore #AB152, RRID:AB_390204, A66). Secondary antibodies used were Alexa Fluor 405 goat anti-rabbit (1:500, Thermo Fisher Scientific #A-31556, RRID:AB_221605, lab antibody code S1), Alexa Fluor 488 goat anti-mouse IgG1 (1:500, Thermo Fisher Scientific #A-21121, RRID:AB_2535764, S7), and Alexa Fluor 568 goat anti-guinea pig (1:500, Thermo Fisher Scientific #A-11075, RRID:AB_2534119, S27). Confocal images were captured on an inverted spinning disk confocal microscope with a 20x, 0.8 numerical aperture air objective. Identical acquisition settings were used within a specific channel for an entire experiment. For all regions, 30 to 50 images were acquired in z from each section at a 0.9 μm step size. 20 contiguous planes were manually selected for analyses. For quantification of axonal innervation, background subtraction in each image plane was performed using the rolling ball algorithm (with a radius of 20 pixels for M1 cortex and a radius of 50 pixels

for dorsal striatum), and the resulting images were binarized using thresholding modules from Python's Scikit-image package. In M1 cortex, both channels were binarized with the Triangle thresholding method. In the dorsal striatum, the NET staining was binarized with the Triangle method and the RFP staining with the Otsu method. The number of positive pixels in each image plane was summated to quantify the total signal. To calculate the number of double-positive RFP and TH somata in the LC and SNc, 20-plane maximum projection z-stack images were created and each channel's brightness and contrast were identically adjusted across images. Double-positive somata were manually counted. To analyze NET signals after 6-OHDA ablation of LC, brightness and contrast were identically adjusted across images. Individual z-stack planes were binarized with the Triangle method, and the number of positive pixels was summated. Representative images for figures were processed with Fiji and are composed of 20-plane maximum intensity projection z-stacks. In Fig. 1b, brightness and contrast in the green (NET) channel were adjusted identically in M1 cortex and striatum while brightness and contrast in the gray (RFP) channel were differentially adjusted to render cortical dopamine axons visible and to prevent saturation of striatal dopamine axons. For representative images in other figures, brightness and contrast of each channel were adjusted linearly and identically.

GRAB$_{NE}$ and GRAB$_{DA}$ experiments in HEK293T cells

HEK293T cells were cultured as previously established[36,37]. Specifically, cells acquired from ATCC (CRL-3216, RRID: CVCL_0063, purchased mycoplasma-free, human cell line of female origin) were expanded and stored as frozen stocks until use. After thawing, the cells were grown in filtered Dulbecco's Modified Eagle Medium (DMEM) supplemented with 10% fetal bovine serum (Atlas Biologicals F-0500-D) and 1% Penicillin-Streptomycin. HEK293T cells were split every 1 to 3 days at a ratio of 1:3 to 1:10. Cell batches were replaced after ~20 passages by thawing a fresh vial from the expanded stock. For puffing experiments, HEK293T cells were plated on 0.1 mm-thick Matrigel-coated glass coverslips (12 mm) at ~10-20% confluency in 24-

well plates. After ~24 hours, cells were transfected with the calcium phosphate method at ~50-60% confluency with 350 ng of pCMV-GRAB$_{NE2h}$ (lab plasmid code p1109, provided by Y.L.)[4] or 200 ng of pCMV-GRAB$_{DA2m}$ (p1110, provided by Y.L.)[2]. Between 24 to 48 hours after transfection, individual coverslips were transferred to a recording chamber perfused with a recording solution containing (in mM) 126 NaCl, 2.5 KCl, 2 CaCl$_2$, 1.3 MgSO$_4$, 1 NaH$_2$PO$_4$, 12 glucose 26.2, and NaHCO$_3$ at 33 to 35 ºC with a flow rate of 2 to 3 mL/min. The recording solution was continuously bubbled with 95% O$_2$ and 5% CO$_2$. Fluorescence imaging was performed using an Olympus BX51WI epifluorescence microscope. Fluorescence signals were excited with a 470 nm LED and digitized with a scientific complementary metal-oxide-semiconductor camera (sCMOS, Hamamatsu Orca-Flash4.0). Data were acquired with a 60x, 0.9 numerical aperture water-immersion objective at 512 x 512 pixels/frame and at 20 frames/s, with an exposure time of 50 ms. Dopamine hydrochloride or noradrenaline bitartrate was dissolved in MilliQ H$_2$O to generate 100 mM stocks. These stocks were then diluted into recording solution to generate 10 µM working solutions and puffed for a 3-second epoch onto the cells using a pulled glass pipette (3 to 5 µm tip diameter) connected to a Picospritzer. Analyses of $\Delta F/F_0$ responses were performed in Python. The fluorescence (F) for each time point encompasses the averaged pixel intensities of the entire 512 x 512 image. Baseline fluorescence (F_0) represents the averaged fluorescence values captured during the 1.5 s window before puffing. $\Delta F/F_0$ was calculated as $(F-F_0)/F_0$ for each time point to generate time series plots. Peak $\Delta F/F_0$ values were then extracted from the time series after puffing and plotted. To generate representative heatmaps, peak fluorescence for each pixel was averaged from a 3.75 s window following the puff. $\Delta F/F_0$ was then calculated for each pixel and plotted in the heatmap images. The resulting images were smoothened with a Gaussian blur (σ = 1).

Stereotaxic Surgeries

Stereotaxic surgeries were performed following previously established methodology[14,16,20,23].

Mice were anesthetized with 5% isoflurane and mounted on a stereotaxic frame. 1.5 to 2% isoflurane was used to maintain stable anesthesia. Following exposure of the skull, a hand drill was used to create a small burr hole for syringe placement. For unilateral and bilateral injections in the dorsal striatum (coordinates relative to bregma: 1.0 mm anterior, ±2.0 mm lateral, 2.5 mm below the dura), adeno-associated viruses (AAVs) were delivered using a syringe coupled to a microinjector pump at a volume of 1 μL with a flow rate of 100 nL/min. Viruses were diluted to a working titer of 10^{11} copies/mL before injection. Mice used for fiber photometry were unilaterally equipped with fiberoptic cannulas (400 μm diameter) in the right dorsal striatum that were placed immediately following AAV delivery (coordinates relative to bregma: 1.0 mm anterior, 2.0 mm lateral, 2.3 mm below the dura) and fixed using quick adhesive dental cement. For unilateral and bilateral viral injections in M1 cortex (coordinates relative to bregma: 1.0 mm anterior, ±1.4 mm lateral, 1.25 mm below the dura) and the LC (coordinates relative to bregma: 5.40 mm posterior, ±1 mm lateral, 3.3 mm below the dura), manually pulled borosilicate glass pipettes (tip diameter 3 to 5 μm) were used for AAV delivery. A volume of 500 nL was delivered at a flow rate of 50 nL/min in M1. For bilateral AAV expression targeted to the LC, 1 μL of virus was injected at a flow rate of 100 nL/min on each side (coordinates relative to bregma: 5.40 mm posterior, ±1 mm lateral, 3.3 mm below the dura). For 6-hydroxydopamine hydrobromide (6-OHDA) injections in the right LC (coordinates relative to bregma: 5.40 mm posterior, 0.75 mm lateral, 3.3 mm below the dura), 1 μL of 6-OHDA (10 μg/μL in PBS containing 0.01% ascorbic acid) was delivered at a flow rate of 100 nL/min with a manually pulled borosilicate glass pipette (tip diameter 3 to 5 μm). Following injections, microinjectors were left in place for 10 minutes to allow the injected volume to settle. Mice were treated for postsurgical pain and were returned to their home cages for a minimum of 14 days before experiments.

Adeno-associated viruses

AAVs were of the AAV9 serotype defined by the capsid, serotypes are included in figures

independent of pseudotyping, and AAVs are available from Biohippo, BrainVTA, WZBioscience and Addgene. AAV9-hSyn-GRAB$_{DA2m}$ (stocks at 1-2 x 10^{12} copies/mL, BioHippo, #BHV12400556-9) and AAV9-hSyn-GRAB$_{NE2h}$ (stocks at 1-2 x 10^{12} copies/mL, BioHippo, #BHV12400441-9) were purchased with permission from Y.L. AAV9-hSyn-nLightG (stocks at 1.4 x 10^{12} copies/mL, produced by the Viral Vector Facility of the University and ETH Zürich, AAV2/9.hSyn.nLightG) was provided by T.P. For photometry, AAV9-hSyn-GRAB$_{NE2h}$ was co-injected with AAV9-CAG-tdTomato (stocks at 1-2 x 10^{13} copies/mL, Addgene, #59462-AAV9).

Slice imaging and analyses

Imaging in acute brain slices was performed as previously established[16,23]. Specifically, mice were deeply anesthetized with isoflurane and decapitated. The brain was dissected out and 250 µm thick brain slices were cut using a vibratome in ice-cold cutting solution containing (in mM) 75 NaCl, 2.5 KCl, 7.5 MgSO$_4$, 75 Sucrose, 1 NaH$_2$PO$_4$, 12 Glucose, 26.2 NaHCO$_3$, 1 Myo-inositol, 3 Na Pyruvic acid, and 1 Na Ascorbic acid. Sagittal slices were prepared for imaging in M1 cortex or dorsal striatum while coronal slices were cut for imaging in the LC. For experiments involving 6-OHDA ablation of the LC, sagittal slices from both hemispheres were cut. After cutting, slices were incubated for 30 minutes at 37 ºC in a recovery solution composed of (in mM) 126 NaCl, 2.5 KCl, 2 CaCl$_2$, 1.3 MgSO$_4$, 1 NaH$_2$PO$_4$, 12 glucose, 26.2 NaHCO$_3$, 1 Myo-inositol, 3 Na Pyruvic acid, and 1 Na Ascorbic acid. Slices were then incubated at minimum for 30 minutes at room temperature. Imaging was performed in a chamber continuously perfused with artificial cerebral spinal fluid (ACSF) containing (in mM) 126 NaCl, 2.5 KCl, 2 CaCl$_2$, 1.3 MgSO$_4$, 1 NaH$_2$PO$_4$, 12 glucose, and 26.2 NaHCO$_3$ at 33 to 35 ºC with a flow rate of 2 to 3 mL/min. All solutions were constantly bubbled with 95% O$_2$ and 5% CO$_2$, and data acquisition was completed within 5 hours of slicing. For Supplemental fig. 4, 1 µM of dihydro-β-erythroidine hydrobromide (DHβE, diluted from 100 mM stock) was included in the recording solution. Fluorescence imaging was performed with an Olympus BX51WI epifluorescence

microscope. A 470 nm LED was used for excitation and the measured signals were digitized with a sCMOS camera (Hamamatsu Orca-Flash4.0). A 4x, 0.13 numerical aperture air objective was used for striatal imaging, while LC and M1 cortex imaging were performed with 10x, 0.30 numerical aperture or 40x, 0.80 numerical aperture water-immersion objectives, respectively. Electrical stimulation was applied using a pulled glass pipette filled with ACSF (3 to 5 µm tip diameter, 0.5 to 1 MΩ). Single stimuli and 20-stimulus 20 Hz trains were delivered at an intensity of 90 µA for 2 to 3 replicates with 2-minute interstimulus intervals using a linear stimulus isolator. A biphasic wave (0.25 ms in each phase) was applied for each stimulus. For Supplemental fig. 2a-d, fluorescence changes in responses to single and train stimuli were assessed before and after wash-on of tetrodotoxin (TTX, 1 µM) for 10 minutes. For Supplemental fig. 2e-h, fluorescence changes in responses to single and train stimuli were assessed before and after wash-on of a cocktail containing 6-Cyano-7-nitroquinoxaline-2,3-dione (CNQX, 10 µm), D-AP-5 (20 µm), SR-95531hydrobromide (gabazine, 10 µM), CGP-55845 hydrochloride (300 nm), atropine (30 nm), and DHβE (1 µm) for 20 minutes. For Supplemental fig. 2i-l, fluorescence changes in responses to single and train stimuli were assessed before and after incubation in ACSF for 20 minutes. Fluorescence images were acquired at 512 x 512 pixels/frame and 50 frames/s with an exposure time of 20 ms. Striatal slice imaging using DHβE was performed at 20 frames/s with an exposure time of 50 ms per frame. Image analyses were performed in Python. For quantification of transients in the dorsal striatum and LC (Figs. 1 and 2, and Supplemental figs. 4, 6, and 8), circular regions of interest (ROIs) with 30- to 50-pixel radii were manually selected in each image time series to calculate time series of $\Delta F/F_0$. The position of each ROI was centered around the visually identified peak signal. The radii of manually selected ROIs were constant for each brain area at 50 pixels for LC and 30 pixels for dorsal striatum. For recordings in M1 cortex shown in Fig. 1 and Supplemental. fig. 2, ROIs were generated from the top 10% of responding pixels in the first 20-stimuli replicate. The resulting mask was then used to calculate $\Delta F/F_0$ in the remaining replicates. M1

cortex recordings in Fig. 3 were analyzed using manually selected circular ROIs with a radius of 100 pixels. For recordings in M1 cortex, LC, and dorsal striatum with nLightG or in the presence of DHβE, bleach correction was performed on raw signals with Python's SciPy's curve fitting module using an exponential decay function. To determine baseline fluorescence (F_0), 500 ms windows before the onset of electrical stimulation were averaged within an ROI. The fluorescence (F) for each time point represents the averaged pixel intensities within each ROI. $\Delta F/F_0$ was then calculated as $(F-F_0)/F_0$ for each time point and averaged to generate the time series plots. Peak $\Delta F/F_0$ values were then extracted from the time series and plotted. This process was also used to create example heat plot images for the time window 280-500 ms after stimulation. The resulting images were smoothened with a Gaussian blur (σ = 1) to generate the example heat plot images for display in the figures. Recordings from control and experimental conditions were processed identically.

Fiber photometry

Fiber photometric recordings in freely moving mice were performed as previously established[16,23]. At 21 days after surgical implantation, the fiberoptic cannula was connected to an optic patch cord, and the mice were allowed to freely roam for 1-hour epochs in a circular arena (43.1 cm diameter, 35.6 cm high) illuminated by infrared light (850 nm, 30 µW/cm^2 as measured from the arena surface). Silicon photodiodes were used to convert fluorescence to electrical signals, which were then amplified by photodiode amplifiers and collected by a multifunction I/O card at 10,000 Hz. 470 nm and 565 nm LEDs (Thorlabs) were used to excite the channels and applied at 157 µW and 17 µW, respectively, and as established before[16]. Output power was chosen to hold the raw fluorescence signals for green and red channels in a similar range, and excitation for each LED was applied in an alternating pattern at 25 Hz. During the 40 ms active period, each excitation channel was on for 10 ms and the average output of each channel was assessed and set according to previously established protocols[23]. For

analyses, the raw photometry signal F was first processed with a low-pass filter at 0.01 Hz to estimate F_0, and $\Delta F/F_0$ was calculated as $(F-F_0)/F_0$ and analyzed from the first 30 minutes of the 1-hour data acquisition. To quantify the fluorescence fluctuations, a 640 ms sliding window was applied to $\Delta F/F_0$ transients to calculate an average of the standard deviation. Brief illuminations (200 ms light pulses, 565 nm LED light source, 50 µW/cm^2 measured at the bottom of the arena) were applied at random time intervals ranging from 60 to 210 s during the 1 h epoch. At the end of the experiment, animals were deeply anesthetized with 5% isoflurane and transcardially perfused with 30 mL PBS followed by 40 mL 4% PFA in PBS. Brains were then extracted and post-fixed in 4% PFA in PBS for 24 hours following perfusion. Brain slices were cut at 50 µm in ice-cold PBS on a vibratome. Sections were mounted on glass slides with a mounting medium containing DAPI. Images of the brain sections were acquired using a slide scanning microscope with a 4x air objective. Cannula positions were determined with respect to a mouse brain atlas[38] and are displayed in Supplemental fig. 5 on schematics drawn from corresponding brain sections.

Statistics

Data are shown as mean ± SEM with * $p < 0.05$, ** $p < 0.01$, *** $p < 0.001$. Data were plotted using Python (Python Software Foundation, 3.11.4), MATLAB (MathWorks R2022b) and/or Prism (GraphPad 10.2.3), and individual data points are included in each figure whenever possible. The number of observations in each experiment was based on previous publications[14,16,23,39] and on trial experiments; no statistical methods were used to predetermine sample sizes. For each experiment, the definitions of n are specified in the figure legends, and sample sizes for each plot are included in each figure legend. For genotype comparisons, the experimenter was blind to genotype while acquiring and analyzing data. Data sets were tested for normality with Anderson-Darling, D'Agostino-Pearson omnibus, Shapiro-Wilk, and Kolmogorov-Smirnov tests. Data sets were tested for variance with the F test for two-group

comparisons and the Brown-Forsythe and Bartlett's tests for three-group comparisons. Data sets that met criteria for normalcy and equal variance across all tests were analyzed using parametric statistical tests. Non-parametric tests were used otherwise. Specifically, two-tailed Mann-Whitney rank-sum tests were used for Figs. 1c, 2e, 2h, 3c, 3g, 3k, and 3o (single stimulus), and Supplemental figs. 3c, 4d, and 7c. Two-tailed Wilcoxon sign-rank tests were used for Figs. 1g and 1j, and Supplemental figs. 2d, 2h, 8d, and 8g. Two-tailed paired t-tests were used for Supplemental fig. 2l. Two-tailed unpaired t-tests were used for Figs. 2k and 3o (20 stimuli), and Supplemental fig. 6f. One-way ANOVA and Dunnet's multiple comparisons post-hoc tests were used for Supplemental fig. 2m. Kruskal-Wallis and Dunn's multiple comparisons tests were used for Supplemental fig. 2n. The specific statistical tests used are also described in each figure legend.
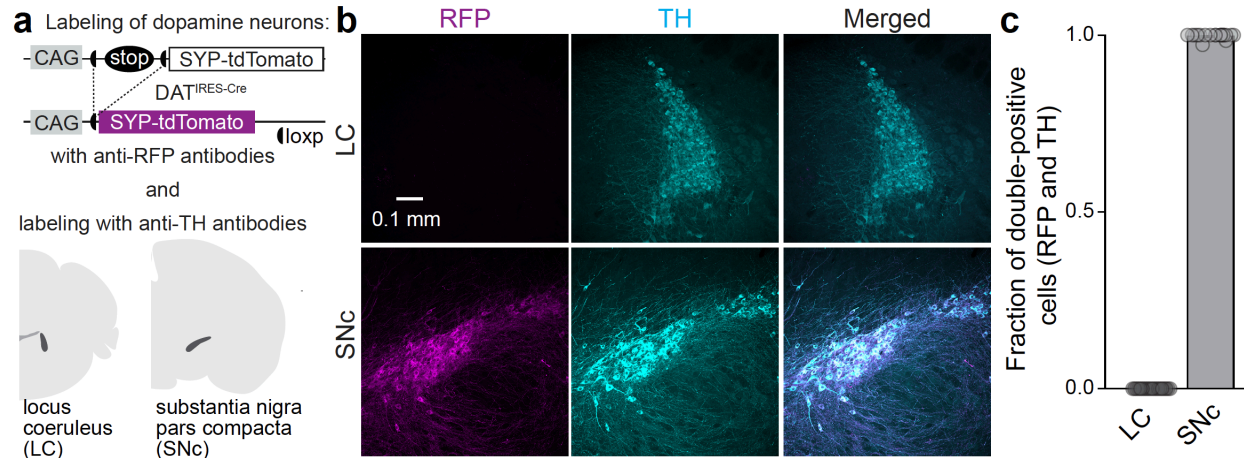
Supplemental figure 1. Assessment of Cre-dependent expression of synaptophysin-tdTomato in DAT^{IRES-Cre} mice

a. Strategy for labeling dopamine and norepinephrine neurons similar to Fig. 1a-c but with staining for tyrosine hydroxylase (TH) followed by analyses of immunofluorescence in locus coeruleus (LC) and substantia nigra pars compacta (SNc).

b, c. Representative confocal images of LC and SNc (b) and quantification of the fraction of cells double positive for RFP and TH (c); LC 20 slices from 4 mice, SNc 20/4.

Data are mean ± SEM. On average, 96 ± 6 cells in LC and 88 ± 6 cells in SNc were positive for TH per image. The observation that there are no double-positive cells in LC indicates that the DAT^{IRES-Cre} line does not express Cre in LC neurons. Hence, the strategy of NET labeling combined with RFP-labeling of SYP-tdTomato in DAT^{IRES-Cre} mice can be used to distinguish norepinephrine from dopamine axons. Both norepinephrine and dopamine neurons express TH.
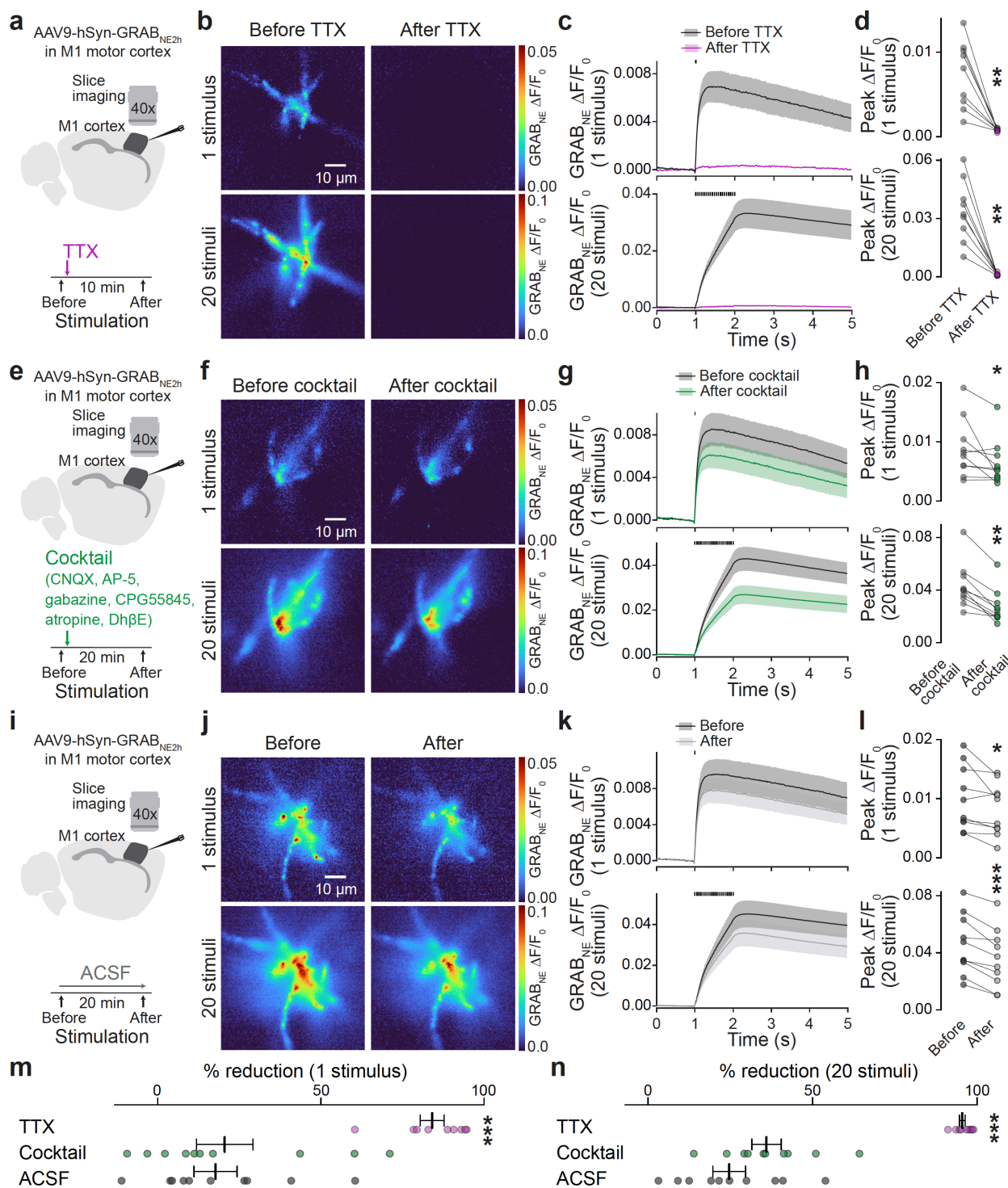
Supplemental figure 2. Pharmacological inhibition of GRAB_{NE} transients in brain slices

a. Schematic of imaging in cortex before and after 10-minute bath application of the sodium channel blocker tetrodotoxin (TTX) to inhibit action potential firing.
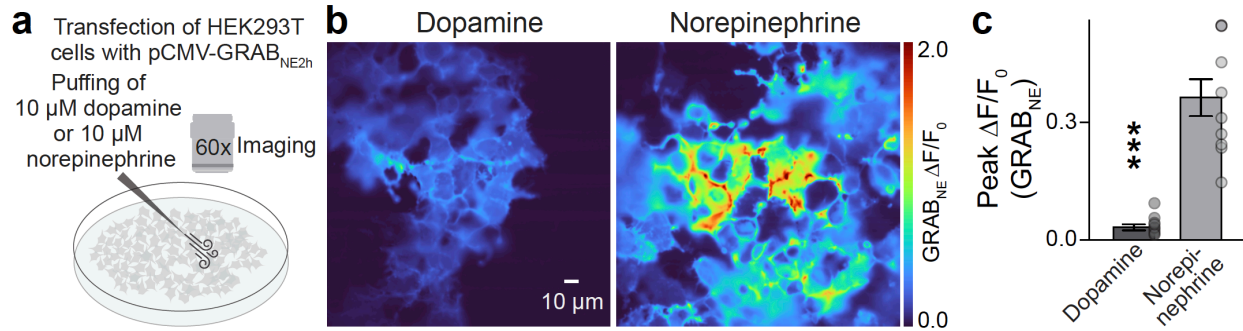
b-d. Representative images of peak GRAB$_{NE}$ fluorescence in response to 1 stimulus or 20 stimuli at 20 Hz before and after TTX wash-on (b) and quantification of GRAB$_{NE}$ $\Delta F/F_0$ time series (c) and peak $\Delta F/F_0$ (d); 9 slices from 3 mice.

e-h. Same as in a-d, but with bath application of a drug cocktail containing CNQX, AP-5, gabazine, CGP-55845, atropine, and DHβE for 20 min; 10/3.

i-l. Same as in a-d, but with incubation in ACSF for 20 min; 10/3.

m, n. Post-hoc assessment of percent reduction in response to 1 stimulus (m) or 20 stimuli (n) comparing incubation in TTX (a-d, 10 min), the drug cocktail (e-h, 20 min), or ACSF (i-l, 20 min); TTX 9/3, cocktail 10/3, and ACSF 10/3. Overall, rundown during drug cocktail application and incubation in ACSF was similar while TTX strongly inhibited the fluorescence changes. Data are mean ± SEM; *** $p < 0.001$, ** $p < 0.01$, * $p < 0.05$, as assessed by: two-tailed Wilcoxon signed-rank tests in d and h; two-tailed paired t-tests in l; one-way ANOVA and Dunnet's multiple comparisons post-hoc tests in m (compared to ACSF); Kruskal-Wallis and Dunn's multiple comparisons tests in n (compared to ACSF).

Supplemental figure 3. Assessment of GRAB$_{NE}$ fluorescence in HEK293T cells

a. Schematic of the experiment in which 10 μM of dopamine or norepinephrine were puffed onto HEK293T cells transfected with pCMV-GRAB$_{NE2h}$.

b, c. Representative peak GRAB$_{NE}$ fluorescence (b) and peak $\Delta F/F_0$ (c); 10 coverslips from 3 transfections each.

Data are mean ± SEM; *** $p < 0.001$, as assessed by two-tailed Mann-Whitney rank-sum test in c.
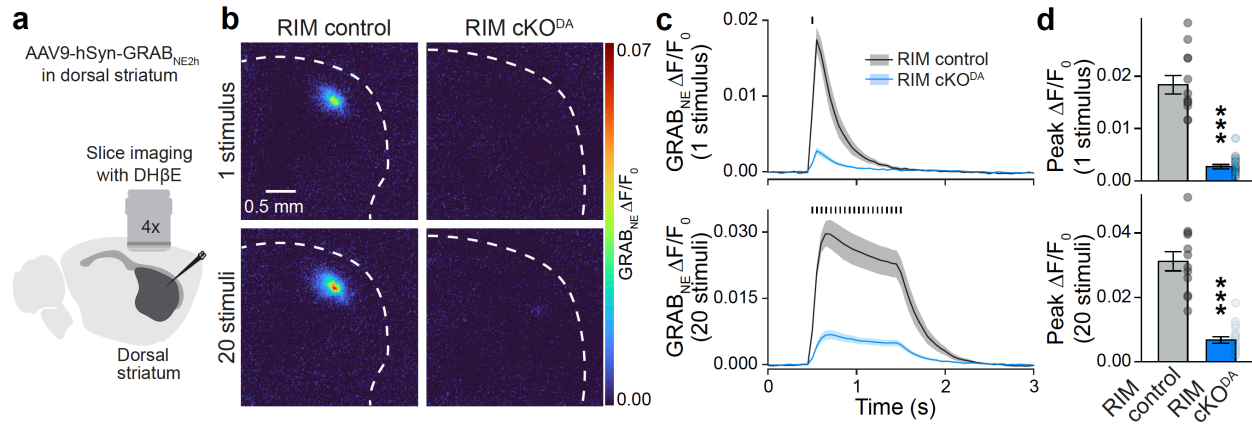
Supplemental figure 4. GRAB$_{NE}$ recordings in striatum in the presence of DHβE

a. Schematic of imaging experiments as in Fig. 2c-e, but in the presence of dihydro-β-erythroidine hydrobromide (DHβE, 1 µM) to block β2-containing nicotinic acetylcholine receptors.

b-d. Representative images of peak GRAB$_{NE}$ fluorescence in response to 1 stimulus or 20 stimuli at 20 Hz (b) and quantification of GRAB$_{NE}$ $\Delta F/F_0$ time series (c) and peak $\Delta F/F_0$ (d); RIM control 12 slices from 3 mice, RIM cKO^{DA} 17/4.

Data are mean ± SEM; *** $p < 0.001$, as assessed by two-tailed Mann-Whitney rank-sum tests in d.
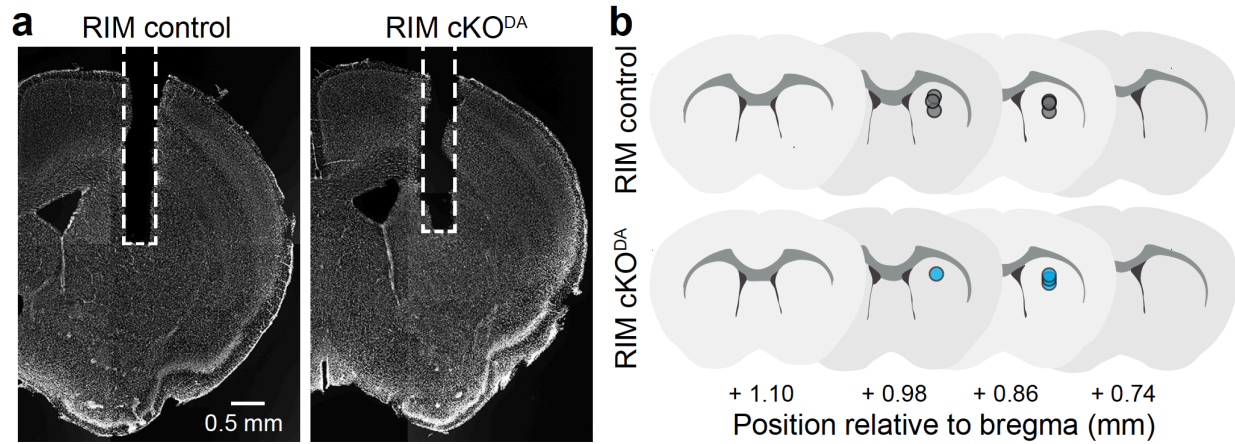
**Supplemental figure 5. Fiberoptic cannula positions**

a. Representative images of coronal sections of mice with fiberoptic cannulas. Coronal sections were imaged with a slide scanner in DAPI-containing mounting medium.

b. Illustration of fiberoptic cannula tip positions of the mice analyzed in Fig. 2k determined relative to a mouse brain atlas[38] and mapped onto schematics drawn from brain sections.
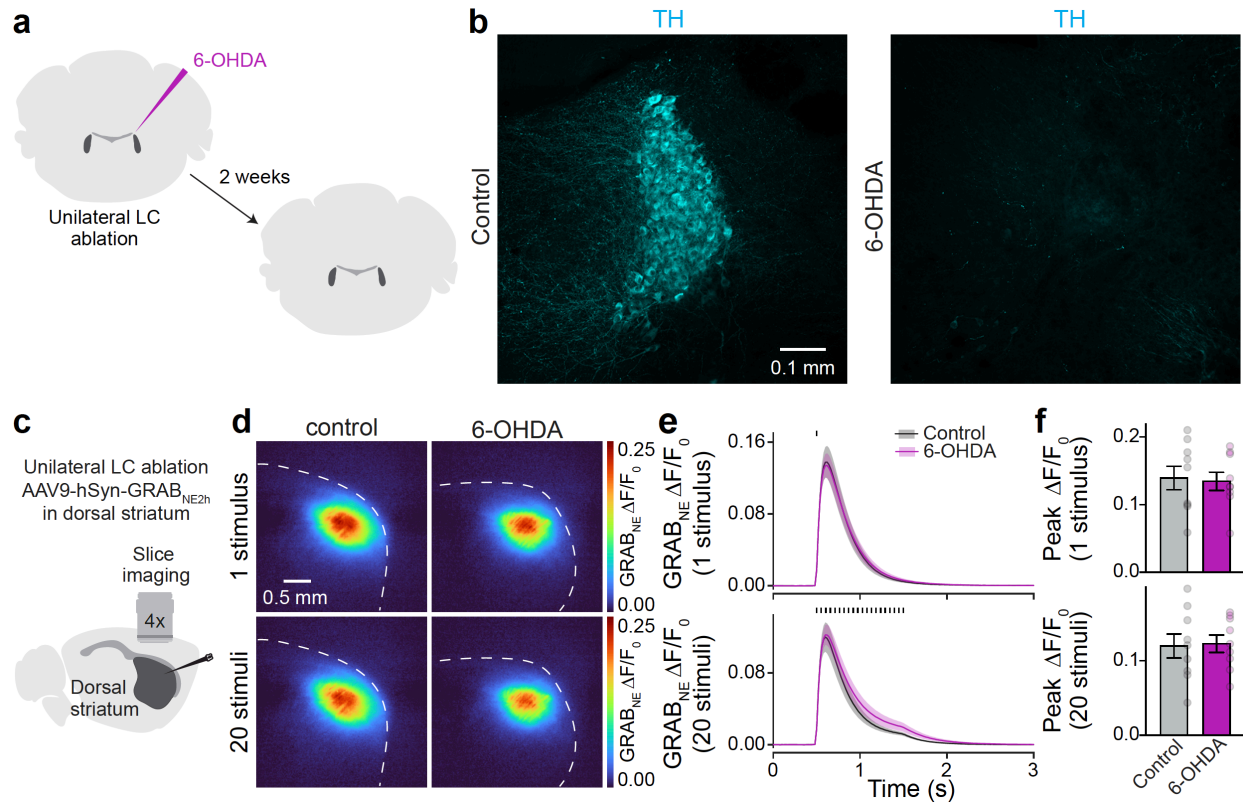
Supplemental figure 6. Striatal GRAB$_{NE}$ responses after 6-OHDA lesion of LC

a. Schematic of unilateral 6-OHDA ablation of LC followed by assessment with confocal microscopy.

b. Confocal images of LC after staining with TH antibodies; a representative image of 4 slices from 4 mice is shown.

c. Schematic of bilateral slice imaging in dorsal striatum expressing GRAB$_{NE}$ with unilateral 6-OHDA ablation of the right LC.

d-f. Representative images of peak GRAB$_{NE}$ fluorescence in response to 1 stimulus or 20 stimuli at 20 Hz in ipsilateral (6-OHDA) and contralateral (control) hemispheres (d) and quantification of GRAB$_{NE}$ $\Delta F/F_0$ time series (e) and peak $\Delta F/F_0$ (f); control 9 slices from 3 mice, 6-OHDA 9/3.
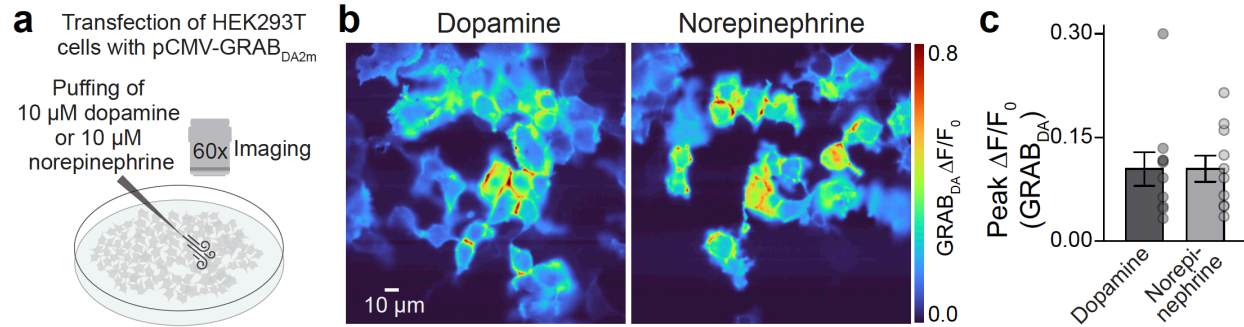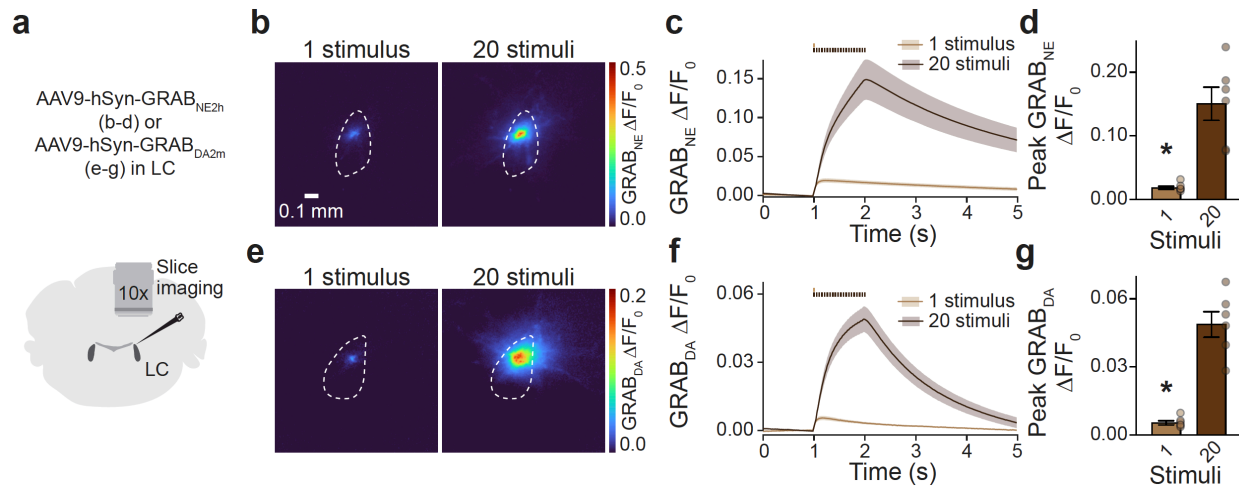
Supplemental figure 7. Assessment of GRAB$_{DA}$ fluorescence in HEK293T cells

a. Schematic of the experiment in which 10 µM of dopamine or norepinephrine were puffed onto HEK293T cells transfected with pCMV-GRAB$_{DA2m}$.

b, c. Representative peak GRAB$_{DA}$ fluorescence (b) and peak $\Delta F/F_0$ (c); 10 coverslips from 3 transfections each.

Data are mean ± SEM.

Supplemental figure 8. Norepinephrine and dopamine sensors in LC

a. Schematic of slice imaging in LC.

b-d. Representative GRAB$_{NE}$ peak fluorescence in response to 1 stimulus or 20 stimuli at 20 Hz in LC (b) and quantification of $\Delta F/F_0$ time series (c) and peak $\Delta F/F_0$ (d); 6 hemispheres from 3 slices from 3 mice.

e-g. As in b-d, but with GRAB$_{DA}$; 6/3/3.

Data are mean ± SEM; * < 0.05 as assessed by two-tailed Wilcoxon signed-rank tests in d and g.

Supplemental text. Studies with GPCR-based sensors in brain areas with dual dopamine and norepinephrine innervation

In the present study, we tested whether GPCR-based dopamine and norepinephrine sensors are specific for their corresponding transmitters in the brain. These sensors have been widely used in brain areas that are innervated by both norepinephrine and dopamine neurons and have been expressed in mice and rats.

Previous studies have used norepinephrine or dopamine sensors in the cortex[3,4,40–50] and in the cerebellum[51], brain areas in which norepinephrine innervation is typically higher in density compared to dopamine innervation[7,10] (Fig. 1a-c). Areas with dopamine and norepinephrine innervation densities that are likely in a similar range[52–56] have also been studied with these sensors, for example the hippocampus[5,57–60], the basolateral amygdala[3,49], the lateral hypothalamus[4,60–62], and the basal forebrain and thalamus[63]. Finally, dually innervated brain areas in which dopamine dominates over norepinephrine[55,64,65] have been characterized with the sensors as well, for example the ventral striatum[1–3,16,49,50,62,66–72] and the ventral tegmental area[49].

Overall, the sensor signals in these brain regions might be due to either dopamine or norepinephrine release. Without cell type- or projection-specific manipulations to remove either dopamine or norepinephrine innervation and/or secretion, it is difficult to conclude which transmitter is detected in dually innervated brain areas when GPCR-based sensors for dopamine or norepinephrine are used.